

VUV-absorption cross section of carbon dioxide from 150 to 800 K and applications to warm exoplanetary atmospheres[★]

O. Venot^{1,2}, Y. Bénilan¹, N. Fray¹, M.-C. Gazeau¹, F. Lefèvre³, Et. Es-sebbar⁴, E. Hébrard⁵, M. Schwell¹, C. Bahrini¹, F. Montmessin⁶, M. Lefèvre^{1,7}, and I. P. Waldmann⁸

¹ Laboratoire Interuniversitaire des Systèmes Atmosphériques, UMR CNRS 7583, Universités Paris Est Créteil (UPEC) et Paris Diderot (UPD), 94010 Créteil Cedex, France
e-mail: olivia.venot@lisa.u-pec.fr

² Instituut voor Sterrenkunde, Katholieke Universiteit Leuven, Celestijnenlaan 200D, 3001 Leuven, Belgium

³ Laboratoire Atmosphères, Milieux, Observations Spatiales (LATMOS), CNRS/IPSL/UPMC, 75252 Paris, France

⁴ Paul Scherrer Institute, Laboratory of Thermal Processes and Combustion, 5232 Villigen PSI, Switzerland

⁵ School of Physics and Astronomy, University of Exeter, EX4 4QL Exeter, UK

⁶ Laboratoire Atmosphères, Milieux, Observations Spatiales (LATMOS), CNRS/IPSL/UVSQ, 478280 Guyancourt, France

⁷ Laboratoire de Météorologie Dynamique, UMR CNRS 8539, Institut Pierre-Simon Laplace, CNRS, Sorbonne Universités, UPMC Université Paris 06, 475005 Paris, France

⁸ University College London, Department of Physics and Astronomy, Gower Street, London WC1E 6BT, UK

Received 2 June 2017 / Accepted 20 September 2017

ABSTRACT

Context. Most exoplanets detected so far have atmospheric temperatures significantly higher than 300 K. Often close to their star, they receive an intense UV photons flux that triggers important photodissociation processes. The temperature dependency of vacuum ultraviolet (VUV) absorption cross sections are poorly known, leading to an undefined uncertainty in atmospheric models. Similarly, data measured at low temperatures similar to those of the high atmosphere of Mars, Venus, and Titan are often lacking.

Aims. Our aim is to quantify the temperature dependency of the VUV absorption cross sections of important molecules in planetary atmospheres. We want to provide high-resolution data at temperatures prevailing in these media, and a simple parameterisation of the absorption in order to simplify its use in photochemical models. This study focuses on carbon dioxide (CO₂).

Methods. We performed experimental measurements of CO₂ absorption cross sections with synchrotron radiation for the wavelength range (115–200 nm). For longer wavelengths (195–230 nm), we used a deuterium lamp and a 1.5 m Jobin-Yvon spectrometer. We used these data in our one-dimensional (1D) thermo-photochemical model in order to study their impact on the predicted atmospheric compositions.

Results. The VUV absorption cross section of CO₂ increases with the temperature. The absorption we measured at 150 K seems to be close to the absorption of CO₂ in the fundamental ground state. The absorption cross section can be separated into two parts: a continuum and a fine structure superimposed on the continuum. The variation in the continuum of absorption can be represented by the sum of three Gaussian functions. Using data at high temperature in thermo-photochemical models significantly modifies the abundance and the photodissociation rates of many species in addition to CO₂, such as methane and ammonia. These deviations have an impact on synthetic transmission spectra, leading to variations of up to 5 ppm.

Conclusions. We present a full set of high-resolution ($\Delta\lambda = 0.03$ nm) absorption cross sections of CO₂ from 115 to 230 nm for temperatures ranging from 150 to 800 K. A parameterisation allows us to calculate the continuum of absorption in this wavelength range. Extrapolation at higher temperature has not been validated experimentally and therefore should be used with caution. Similar studies on other major species are necessary to improve our understanding of planetary atmospheres.

Key words. molecular data – methods: laboratory: molecular – planets and satellites: atmospheres

1. Introduction

The more than three thousand exoplanets detected in the last twenty years have revealed to us the diversity of worlds that exist in the Universe in terms of mass, radius, orbital distance, atmospheric composition, etc. Spectroscopic observations performed during transit allow us to characterise the atmospheres of warm short-orbital distance planets, whereas direct imaging is used to observe young long-orbital distance planets. Whatever the technique used, the exoplanetary atmospheres that are

observable are warm ($T \gtrsim 500$ K). The use of physico-chemical data (e.g. infrared (IR) molecular line lists, ultraviolet (UV) absorption cross sections, chemical reaction rates, branching ratios) not corresponding to the high temperatures of these atmospheres are large sources of error in the understanding of these planets (Liang et al. 2003, 2004). In a collaborative white paper, Fortney et al. (2016) point out several areas where experimental work on molecular data at high temperatures is required in order to improve models used in exoplanet science. With the future space- or ground-based telescopes that will be developed in the coming years (e.g. James Webb Space Telescope (JWST), Extremely Large Telescope (ELT)), investigating these research fields has become urgent.

[★] The data presented in Fig. 1 are only available at the CDS via anonymous ftp to cdsarc.u-strasbg.fr (130.79.128.5) or via <http://cdsarc.u-strasbg.fr/viz-bin/qcat?J/A+A/609/A34>

The need for appropriate data to study planetary atmospheres can also be found much closer to us, in our solar system. In the atmospheres of Mars, Venus, or Titan for instance, UV radiation penetrates in regions around 150 K. While these bodies have been known and studied for several decades, there is still a lack of physico-chemical data at low temperatures.

We aim at improving models of planetary atmospheres by determining vacuum ultraviolet (VUV) absorption cross sections of important molecules in a wide temperature range. In this paper, we focus specifically on carbon dioxide (CO₂). The atmospheres of Mars and Venus being mainly composed of CO₂ (greater than 95%), this molecule plays a primary role in the photochemistry of these two planets. The VUV absorption cross section of CO₂ is therefore essential data for calculating photodissociation rates in photochemical models (Lefèvre et al. 2004; Montmessin et al. 2011), and also necessary in order to analyse the spectrometric data acquired by current spatial instruments such as Spectroscopy for Investigation of Characteristics of the Atmosphere of Mars (SPICAM, mission Mars Express), Imaging Ultraviolet Spectrograph (IUVS, mission MAVEN), or Spectroscopy for Investigation of Characteristics of the Atmosphere of Venus (SPICAV, mission Venus Express). Even if exoplanets composed mainly of CO₂ have not yet been detected, they must probably exist; the presence of CO₂ has been inferred in several observations (e.g. Swain et al. 2009b,a; Madhusudhan & Seager 2009; Madhusudhan et al. 2011), proving that this species is important in exoplanet atmospheres.

It has already been known that the VUV absorption cross section depends on temperature. The first experiments performed at temperatures different from 298 K were performed by Lewis & Carver (1983). They determined the cross section of CO₂, $\sigma_{\text{CO}_2}(\lambda, T)$, at 200, 300, and 370 K in the wavelength range 120–197 nm. They observed an increase in the absorption cross section with the temperature at long wavelengths. Several years later, Yoshino et al. (1996) confirmed this result by measuring $\sigma_{\text{CO}_2}(\lambda, T)$ in the range 118.7–175.5 nm at 195 and 295 K. These measurements were completed by Parkinson et al. (2003) and Stark et al. (2007) who studied the ranges 163–200 nm and 106.1–118.7 nm, respectively, at these two temperatures.

Experimental measurements down to 195 K exist, but this temperature does not correspond to the ~150 K at which a large fraction of the CO₂ photodissociations occurs in the atmospheres of Mars and Venus (e.g. Smith 2004; Zasova et al. 2007). In the absence of data corresponding to this temperature, atmospheric models usually adopt one of the following two solutions: 1) extrapolating the coldest VUV absorption cross section known (i.e. 195 K) to lower temperatures assuming the same variation as between 195 and 298 K, and 2) assuming that no thermal dependence exists for temperatures lower than 195 K. By simplicity, the second option is the mostly commonly chosen. Subsequently, both methods give a highly uncertain absorption cross section at 150 K. A third method consists of modelling the absorption cross sections using theoretical calculations based on ab initio potentials. To our knowledge it is rarely used in atmospheric models.

Concerning the high-temperature domain, some measurements have also been performed in the past. Zuev & Starikovskii (1990) measured the absorption of CO₂ from 190 to 350 nm between 1000 and 4300 K. Later, Jensen et al. (1997) performed measurements in the 230–355 nm range at four temperatures between 1523 and 2273 K. Schulz et al. (2002) also acquired data for CO₂ at nine temperatures between 880 and 3050 K in the wavelength range of 190–320 nm. Oehlschlaeger et al. (2004) reached higher temperatures (4500 K), but determined

$\sigma_{\text{CO}_2}(\lambda, T)$ at only four wavelengths (216.5, 244, 266, and 306 nm). They determined a semi-empirical formula to fit their data. More recently, Venot et al. (2013) published the first VUV absorption data of CO₂ for wavelengths lower than 190 nm at high temperatures. They presented measurements performed between 300 and 550 K in the (115–200 nm) wavelength range, as well as data between 465 and 800 K in the 190–230 nm region. From this dataset, an empirical law was determined to calculate the absorption cross section of CO₂ between 170 and 230 nm. The comparison of those data with the results published by Schulz et al. (2002) showed a disagreement, which might be due to an overestimation of the temperature in the measurements or an underestimation of the absorbance (see, Venot et al. 2013, for a more detailed discussion). Recently, Grebenshchikov (2016) analysed the temperature dependence of the absorption cross section of CO₂ for wavelengths lower than 250 nm using a first principles model and found a very good agreement with the results of Venot et al. (2013).

We present here a complete dataset for the absorption of CO₂ from 150 to 800 K in the range 115–230 nm. We completed the previous measurements of $\sigma_{\text{CO}_2}(\lambda, T)$ and improved the data processing. The results presented in Venot et al. (2013) have thus been reevaluated. We fitted all the data with Gaussian functions, which allowed us to determine a parameterisation of the $\sigma_{\text{CO}_2}(\lambda, T)$ continuum valid for the entire wavelength range studied. In Sect. 2, we present our experimental set-up and our procedures. The results of the measurements are shown in Sect. 3, and applications to high-temperature atmospheric models are presented in Sect. 4. Finally, the main conclusions are summarised in Sect. 5.

2. Experimental methods and procedures

2.1. Measurements

Data have been acquired during three campaigns of measurements: two at the synchrotron radiation facility BESSY¹ in July 2011 and June 2014, and one in the Laboratoire Interuniversitaire des Systèmes Atmosphériques (LISA) in May 2012. Experimental conditions in terms of temperature, pressure, and wavelength studied during each campaign are summarised in Table 1. All the high-temperature measurements have been performed on the same experimental set-up (described in detail in Venot et al. 2013), except that the optical path length varied: 133 cm in 2011, 147 cm in 2012, and 143.9 cm in 2014. To summarise, our set-up is composed of a cylinder cell with a length of 120 cm, placed in an oven. At the entrance of the cell, a cross is mounted in order to connect the gas injection disposal and the MKS Baratron® capacitance manometers (range 10⁻⁴–1 mbar and 1–1000 mbar). A Mg-F₂ window is placed at the beginning of the cross. The other extremity of the cell is closed by a Mg-F₂ window and a solar blind photomultiplier measured the VUV radiation intensity. The optical path length is the distance between the two Mg-F₂ windows, which represents the absorption cell. The uncertainty on the temperature for the high-temperature measurements is 5% (see discussion in Sect. 2.2.1). For the measurements at temperatures lower than 300 K, the experimental set-up is different and is described in detail in Ferradaz et al. (2009). Briefly, the cell is surrounded by a double wall in which liquid nitrogen is flowing, which allows the temperature of the gas contained in the cell to decrease. The temperature is measured thanks to a thermocouple

¹ Berliner Elektronenspeicherring-Gesellschaft für Synchrotronstrahlung.

Table 1. Experimental conditions for each campaign of measurement.

T (K)	λ (nm)	Pressure (mbar)	Period	Facility
150	115–200	0.2–3	June 2014	BESSY
170	115–200	0.3–15	June 2014	BESSY
195	115–200	0.4–400	June 2014	BESSY
230	115–200	0.3–491	June 2014	BESSY
300	115–200	0.25–6.1	July 2011	BESSY
420	115–200	0.40–7.6	July 2011	BESSY
500	115–200	0.40–8.2	July 2011	BESSY
585	115–200	0.53–5.2	June 2014	BESSY
	195–230	73–700	May 2012	LISA
700	115–200	0.52–7.4	June 2014	BESSY
	195–230	95–330	May 2012	LISA
800	115–200	0.40–8.5	June 2014	BESSY
	195–230	30–398	May 2012	LISA

fixed on the inside wall of the cell. We observed a temperature gradient in the cell, leading to an uncertainty on the temperature, $\Delta T = \pm 5$ K. The length of the cell is 108.4 cm, so the total optical path length is 116.8 cm. The uncertainty on the optical path length, ΔL , is lower than 0.1 cm.

For all the temperatures studied, spectra were recorded at a minimum of three different pressures between 0.2 and 700 mbar to check the reproducibility of our measurements. Pressure was measured with two MKS Baratron® capacitance manometers, leading to an uncertainty of 1% corresponding to the precision of the acquisition. The pressure used for each measurement was adapted to the absorption of the gas which varies by several orders of magnitude over the entire wavelength range. This variation forced us to divide the wavelength range into 2 or 3 subranges in order to obtain acquisitions not saturated, with transmission between 10 and 90%. The resolution of the data is $\Delta\lambda = 0.03$ nm.

The total uncertainty on the absorption cross sections is dominated by the uncertainties on the temperature and the pressure of the gas. Comparing the spectra we obtained at different pressures and using a different temperature in the data processing, we estimated it to be about 10%.

2.2. Data processing

2.2.1. Temperature and wavelength calibration

In Venot et al. (2013), we explained that the temperature of the gas is not constant over the entire optical pathway during our high-temperature measurements. This important gradient of temperature can be modelled by a symmetrised inverse exponential function (Eq. (2) in Venot et al. 2013). In Venot et al. (2013), the data were processed considering that the measured absorption corresponded to a gas at a mean temperature T_{mean} . This procedure led to a doubtful behaviour of the absorption cross section of CO₂ between 134 and 150 nm. In this range only, the high-temperature absorption cross sections were lower than they were at 300 K. By studying another molecule (NH₃, Venot et al., in prep.), we realised that this approximation was not correct. In fact, the absorption is dominated by the portion of the gas at the highest temperature. Thus, we have reprocessed here all our data considering that the gas was at the maximum temperature T_{max} on all the optical pathways. The value of T_{max} depends only on the temperature set by the oven (T_{set}) and can be calculated with the formula established in Venot et al. (2013):

$$T_{\text{max}} = 0.53 \times T_{\text{set}} + 181. \quad (1)$$

With this new procedure, a decrease in the absorption in the range 134–150 nm can no longer be observed. All the data presented here have been calculated considering T_{max} . We note that this is applicable only for the measurements at $T > 300$ K.

Concerning the wavelength calibration, we used the absorption cross sections of CO₂ at ambient temperature published by Yoshino et al. (1996), Parkinson et al. (2003), and Stark et al. (2007).

2.2.2. Carbon monoxide

We observed the signature of carbon monoxide (CO) in some of our highest temperature raw data ($T_{\text{max}} > 585$ K). The presence of this molecule in our spectra is due to the thermal decomposition of CO₂, which is catalysed by wall reactions. Using two CO₂ spectra at the same temperature in which CO appeared with different intensities, we isolated the spectral signature of CO. Then we subtracted the CO feature, applying a correction factor that depended on the temperature and the initial amount of CO₂ in the cell. This factor was estimated visually in order to remove completely the CO features without modifying the normal shape of CO₂ spectra. The amount of CO in the cell represents less than 1% of the total amount of gas.

2.2.3. Calculation of the absorption cross section

Absolute photoabsorption cross sections can be calculated using the Beer-Lambert law

$$\sigma = \left(\frac{1}{nL} \right) \times \ln \left(\frac{I_0}{I} \right), \quad (2)$$

where σ is the absorption cross section (cm²), I_0 the light intensity transmitted with an empty cell, I the light intensity transmitted through the gas sample, L the absorption path length (cm), and n the volume density of the gas (cm⁻³), following the relation $P = nk_{\text{B}}T$, where T and P are the temperature (K) and the pressure (Pa) of the sample, respectively, and k_{B} the Boltzmann constant.

3. Results and discussion

3.1. Photoabsorption cross section from 115 nm to 230 nm

We obtained the absorption cross section of CO₂ between 150 and 800 K (Fig. 1), which shows that the temperature dependency of the absorption depends on the wavelength. Around Lyman α , the cross section varies by two orders of magnitude between the two extreme temperatures, whereas between 130 and 150 nm the variation of the absorption is less important (<factor 10 and sometimes almost identical). For wavelengths >160 nm, the deviation of the absorption cross section becomes more pronounced as the wavelength increases. It can also be seen that the absorption cross section does not decrease in the same proportion at low temperature as it increases at high temperature. The difference between the four absorption cross sections at low temperature ($T < 300$ K) is relatively small. At 175 nm for instance, there is only a factor 3.75 between those at 150 K and 300 K. As the temperature decreases the absorption cross section varies less and less, and it seems that a lower limit for the absorption cross section is reached at 150 K. This can be explained by the fact that around this temperature, almost all the molecules are in the vibrational ground state and thus the population of the vibrational levels no longer changes. Assuming a

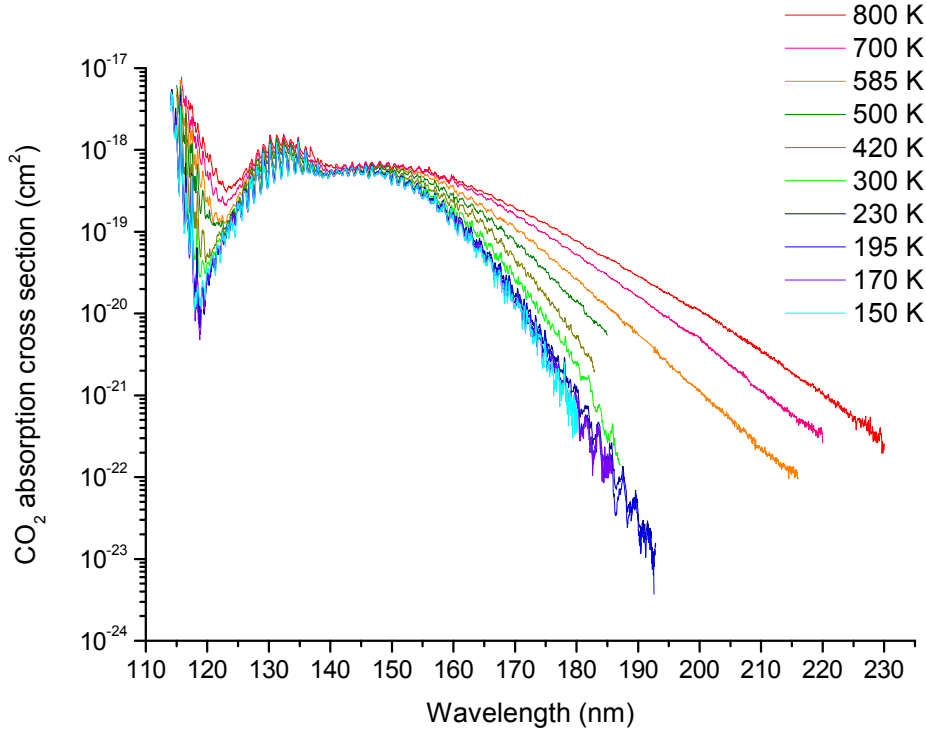


Fig. 1. Absorption cross section of CO₂ (cm²) at temperatures between 150 and 800 K.

Maxwell-Boltzmann distribution between two levels of energy only (i.e. neglecting the higher levels of excitation), we calculate that 4% of the population of the fundamental level is in the first energy level ($\nu = 667 \text{ cm}^{-1}$) at 300 K, whereas at 150 K this ratio is lower than 0.2%.

To analyse in detail the behaviour of the absorption cross section with the temperature, we separated each dataset into two parts: the continuum, and the fine structure superimposed on the continuum. The fine structure contains all the small peaks (with a spectral width of $\sim 1 \text{ nm}$) corresponding to vibrational energy transitions, and the continuum is the baseline that passes through the minima of all these small peaks. At each temperature, we integrated the two components over the entire wavelength range and compared the values. As seen in Fig. 2, when the temperature increases, the contribution of the fine structure to the total absorption decreases. We consider that this contribution of the fine structure becomes negligible for $T > 500 \text{ K}$ as it represents less than 20% of the absorption due to the continuum. We note that what we call the “continuum” is in reality overlapping rovibrational transitions separated by very small energy gaps (Grebenshchikov 2013).

In this paper, we focus on the analysis of the continuum, and on the implication of these new data for high-temperature atmospheric studies. The analysis of the fine structure is in progress and will be presented in a forthcoming paper, with applications to low-temperature atmospheric studies.

3.2. Analysis of the continuum of the absorption

To facilitate the use of these data in atmospheric models, we determined a parameterisation to model the absorption cross section continuum. We found that the continuum of the absorption cross section, hereafter $\sigma_{\text{cont}}(\lambda, T)$, can be represented as the sum of three Gaussian functions:

$$\sigma_{\text{cont}}(\lambda, T) = \sigma_1(\lambda, T) + \sigma_2(\lambda, T) + \sigma_3(\lambda, T). \quad (3)$$

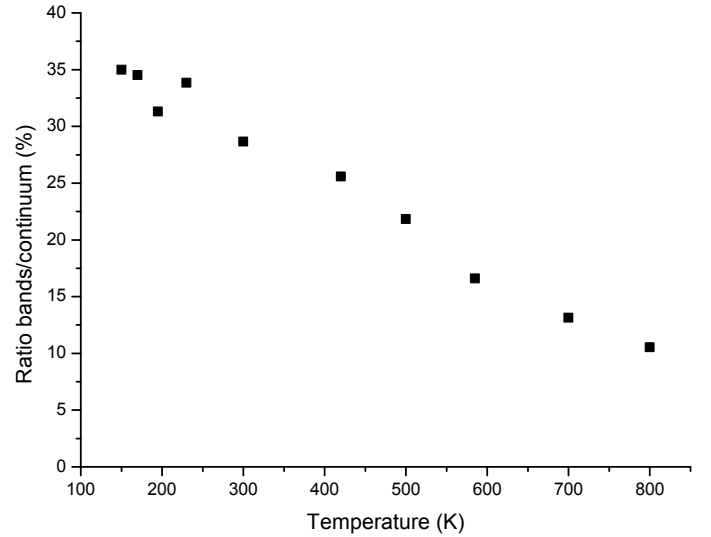


Fig. 2. Thermal evolution of the ratio between the integrated absorption due to the fine structure and that due to the continuum.

Our approach is consistent with the fast dissociation of CO₂ after the VUV excitation and with the so-called reflection principle (Herzberg 1989, p. 392; Schinke 1995, p. 110–112), which essentially approximates the absorption spectrum of each participating electronic state in terms of a Gaussian whose parameters are controlled by the electronic ground state and the properties of each potential in the Franck-Condon region.

For convenience, we expressed each Gaussian function σ_i using the wavenumber ν (cm⁻¹), instead of the wavelength λ ($\lambda = 1/\nu$). We obtained the expression

$$\sigma_i(\lambda, T) = \sigma_i(\nu, T) = A_i(T) \times \exp\left(-\frac{(\nu - \nu_{ci})^2}{2 \times s_i(T)^2}\right), \quad (4)$$

where $A_i(T)$ is the amplitude (cm²), $s_i(T)$ the standard deviation (cm⁻¹), and ν_{ci} the position centre of the Gaussian i (cm⁻¹). The standard deviation is linked to the full width at half maximum (FWHM) according to $FWHM(T) = 2\sqrt{2\ln 2} \times s_i(T)$. To determine the parameterisation, we proceeded in two steps. First, for each temperature we fitted the continuum of absorption with the sum of three Gaussian functions. These fits are called hereafter ‘‘individual fits’’. Then, we traced the parameters (position centres, amplitudes, standard deviations of the three Gaussian functions) of these individual fits in order to determine their variations with the temperature.

For the three Gaussians, the positions of the centres (ν_{ci}) do not vary with the temperature and are equal to $\nu_{c1} = 88\,574$ cm⁻¹ (~ 112.9 nm), $\nu_{c2} = 76\,000$ cm⁻¹ (~ 131.58 nm), and $\nu_{c3} = 68\,000$ cm⁻¹ (~ 147.06 nm). These values are quite close to the positions of the electronic states $1^1\Sigma_u^+$, $1^1\Pi_g$, and $1^1\Delta_u$, respectively (Cossart-Magos et al. 1987; Grebenshchikov 2013, and references therein). For the first peak, the amplitude was fixed at $A_1 = 50 \times 10^{-19}$ cm² for all the temperatures. Consequently, only the standard deviation $s_1(T)$ depends on the temperature. We determined that the variation of $s_1(T)$ could be fitted by the decreasing exponential function (see Fig. 3):

$$s_1(T) = 877.36 + 10\,947.81 \times \exp\left(-\frac{1382.63}{T}\right). \quad (5)$$

For the two other Gaussians, the amplitudes $A_2(T)$ and $A_3(T)$ vary with the temperature. As can be seen in Figs. 4 and 5, these variations can be fitted with a decreasing exponential function (Eq. (6)) and a linear function (Eq. (7)), respectively:

$$A_2(T) = \left(3.58 + 9.18 \times \exp\left(-\frac{580.92}{T}\right)\right) \times 10^{-19} \quad (6)$$

$$A_3(T) = (4.09 + 0.0022 \times T) \times 10^{-19}. \quad (7)$$

Concerning the standard deviations, their variations with respect to temperature are very well fitted by decreasing exponential functions (Eqs. (8) and (9)):

$$s_2(T) = T \times (2.78 + 49.52 \times \exp(-0.00654 \times T)) \quad (8)$$

$$s_3(T) = T \times (8.17 + 46.12 \times \exp(-0.00813 \times T)). \quad (9)$$

From Eqs. (3) and (4), these parameterisations allow us to calculate the continuum of the absorption cross section of CO₂ at any wavelength and any temperature in the ranges (115–230 nm) and (150–800 K). The continua determined from the experimental data and from the analytical formulation are represented in Fig. 6 for all the temperatures between 150 and 800 K; the parameterisation gives very good results, close to the experimental data. On average, the mean deviation between the experimental data and the parameterisation is about 15%.

3.3. Extrapolation at temperatures >800 K

We used Eq. (3) to extrapolate absorption data to higher temperatures (Fig. 7). It is clear that as long as the temperature increases, the wings of the Gaussian functions broaden and the troughs between the three peaks disappear. We compared our results with the parameterisations published by Schulz et al. (2002) and Oehlschlaeger et al. (2004) for the wavelengths longer than 190 nm, but found a disagreement. For one given temperature, the absorption cross sections determined using their coefficients

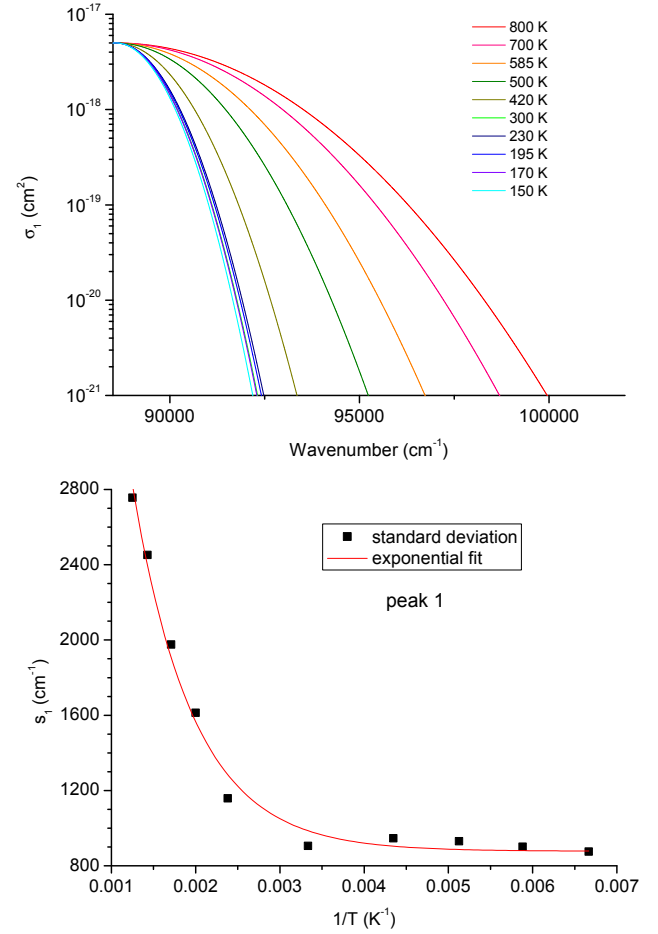


Fig. 3. Top: analytical representation of the first peak of $\sigma_{\text{cont}}(\lambda, T)$ with a Gaussian function, $\sigma_1(\lambda, T)$, centred at $88\,574$ cm⁻¹ for temperatures between 150 and 800 K. Bottom: variation of the standard deviation $s_1(T)$ of the first Gaussian function as a function of $1/T$. The variation can be fitted by a decreasing exponential function.

is lower than our results. To obtain an absorption cross section compatible with our results with their parameterisation, the temperature has to be increased by a factor of ~ 1.5 . This conclusion is similar to what we found in Venot et al. (2013). The discrepancy between our results and theirs can have several origins. It might be due to an overestimation of the temperature or an underestimation of the absorbance in Schulz et al. (2002) and Oehlschlaeger et al. (2004). It has also been pointed out by Oehlschlaeger et al. (2004) that the average mole fraction of CO₂ during the experiments of Schulz et al. (2002) was calculated with a kinetic mechanism (i.e. GRIMEch 3.0) that overestimated the thermal decomposition of CO₂, leading to too low abundances of CO₂ and thus too large absorption cross sections. Grebenshchikov (2016), who also noticed a difference in the temperature scale with Oehlschlaeger et al. (2004) (by ~ 300 K), suggested that this discrepancy could find its origin in some assumptions made in his current model, but also in the development of local vibrational temperature regions in the experiments of Oehlschlaeger et al. (2004). These local regions could have an impact on the absorption cross sections. The vibrational relaxation time, which has not been measured, might be different in our experiments and in Oehlschlaeger et al. (2004).

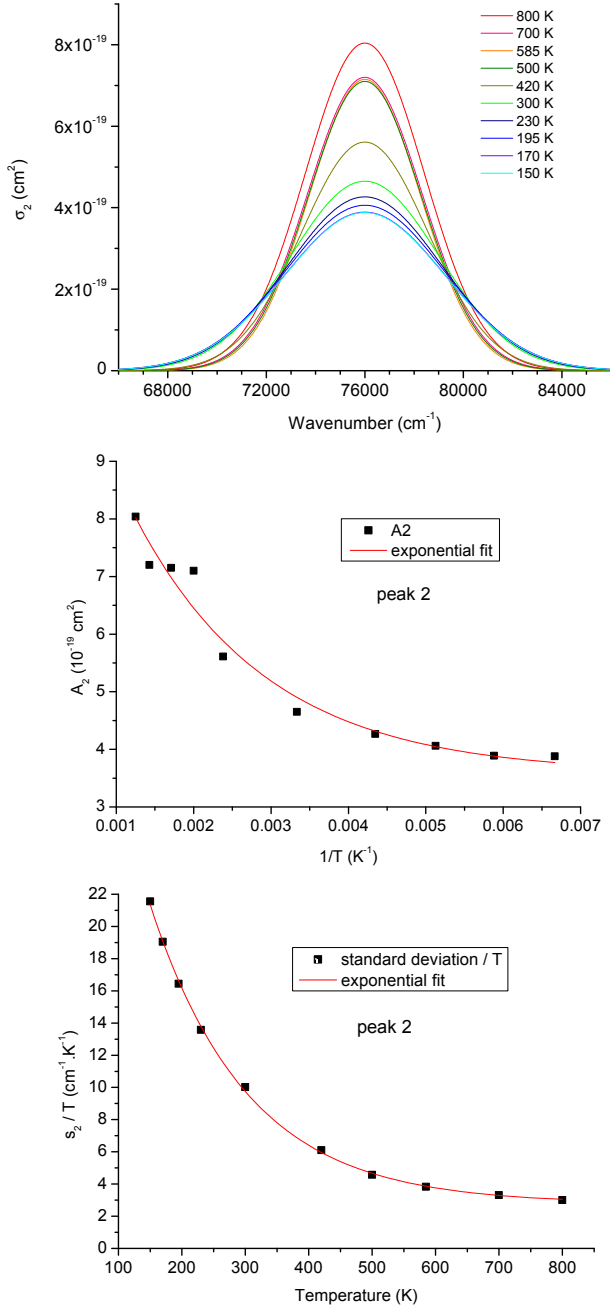


Fig. 4. *Top:* analytical representation of the second peak of $\sigma_{\text{cont}}(\lambda, T)$ with a Gaussian function, $\sigma_2(\lambda, T)$, centred at 76 000 cm⁻¹ for temperatures between 150 and 800 K. *Middle:* variation of the amplitude $A_2(T)$ of the second Gaussian function as a function of $1/T$. The variation can be fitted by a decreasing exponential function. *Bottom:* variation of the standard deviation $s_2(T)/T$ of the second Gaussian function as a function of the temperature. The variation can be fitted by a decreasing exponential function.

4. Application to warm exoplanet atmospheres

4.1. Model

4.1.1. One-dimensional neutral chemical model

We used our 1D thermo-photochemical model to study the effect of the absorption cross sections of CO₂ at high temperature on the chemical composition of exoplanetary atmospheres. Our goal here was not to model a real planet and predict future observations, but only to quantify the effect of the new data

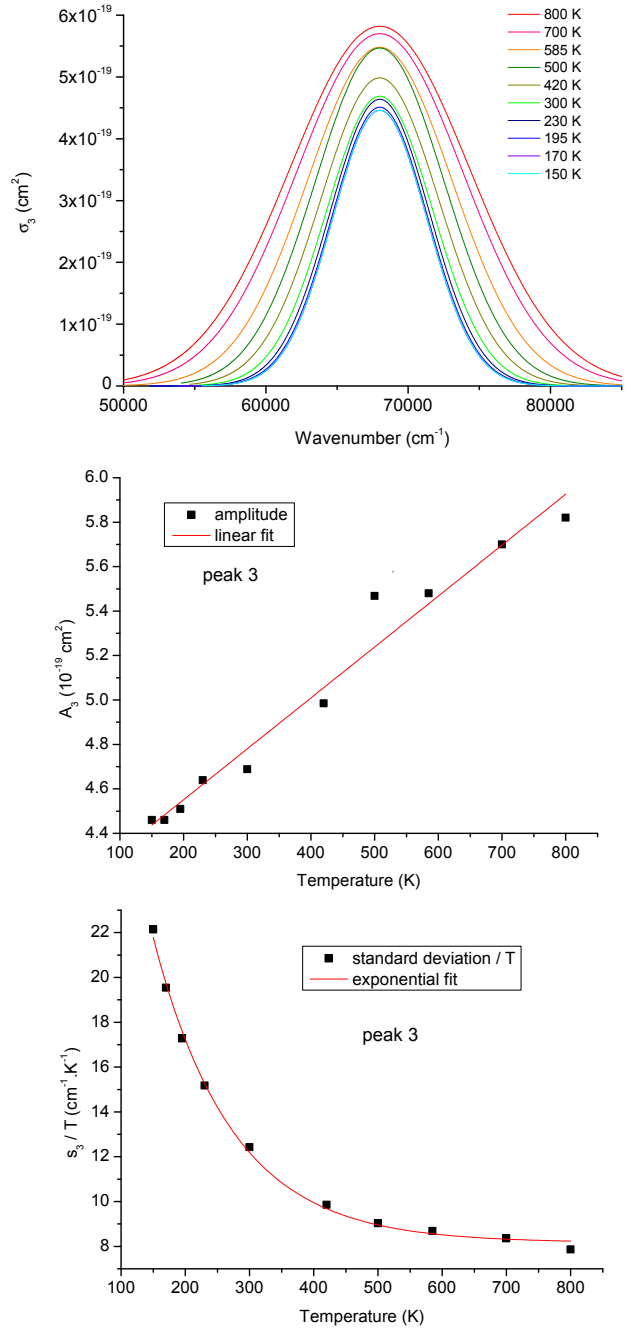


Fig. 5. *Top:* analytical representation of the third peak of $\sigma_{\text{cont}}(\lambda, T)$ with a Gaussian function, $\sigma_3(\lambda, T)$, centred at 68 000 cm⁻¹ for temperatures between 150 and 800 K. *Middle:* variation of the amplitude A_3 of the third Gaussian function as a function of the temperature. The variation can be fitted by a linear function. *Bottom:* variation of the standard deviation $s_3(T)/T$ of the third Gaussian function as a function of the temperature. The variation can be fitted by a decreasing exponential function.

absorption cross section of CO₂ on the atmospheric composition predicted by chemical models. Our 1D time-dependent model is very well adapted to the study of warm atmospheres thanks to the chemical scheme it uses. This scheme has been validated experimentally in large ranges of pressure and temperature ([0.01–100] bars and [300–2500] K). It contains 105 species made of H, C, O, and N and linked by 1920 neutral-neutral reactions. To this validated chemical scheme, we added 55 photolysis reactions. Because our core scheme is a non-optimised network (i.e.

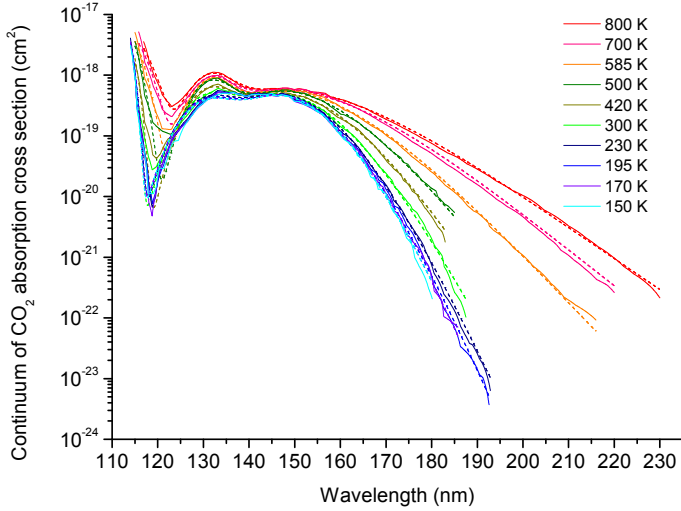


Fig. 6. Continuum of CO₂ absorption cross section (cm²) measured between 150 K and 800 K (full lines). The continuum can be fitted by a sum of three Gaussian functions (dashed lines).

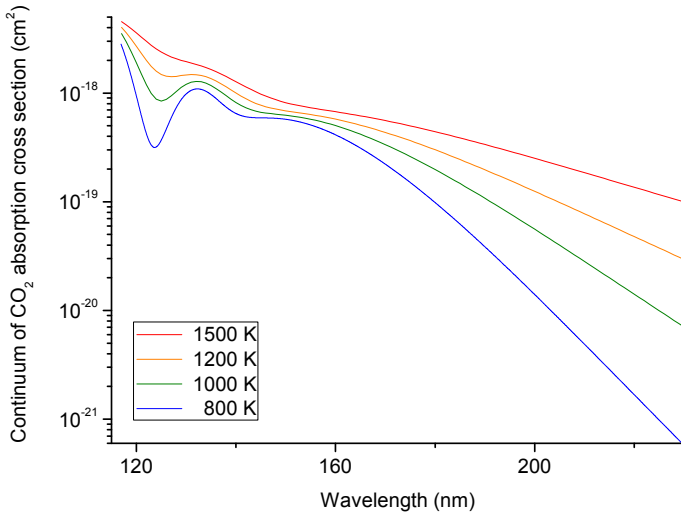


Fig. 7. Continuum of CO₂ absorption cross section extrapolated to 1000 K (green), 1200 K (orange), and 1500 K (red). $\sigma_{\text{cont}}(\lambda, 800)$ (blue) is shown for comparison.

the reaction rate coefficients are those recommended by kinetics databases and have not been modified to fit experiments), the addition of these photolysis reactions does not call into question the validation of the core scheme (see Venot et al. 2012, and references therein). An experimental validation of the whole scheme with photolysis processes would be ideal but represents a challenge given the lack of knowledge to date on high-temperature photolysis data. We used solar C/N/O relative abundances, but increased the metallicity by a factor of 100 compared to the solar metallicity (Asplund et al. 2009), as high metallicity is probable in warm gaseous atmospheres (e.g. Fortney et al. 2013; Moses et al. 2013; Agúndez et al. 2014). The consequence is an increase in the abundance of CO₂ by approximately 4 orders of magnitude compared to solar metallicity, resulting in molar fractions of CO₂ (y_{CO_2}) of 6×10^{-3} and 6×10^{-4} at 1 mbar for the two atmospheres studied here, at 800 K and 1500 K, respectively (see Sect. 4.1.2).

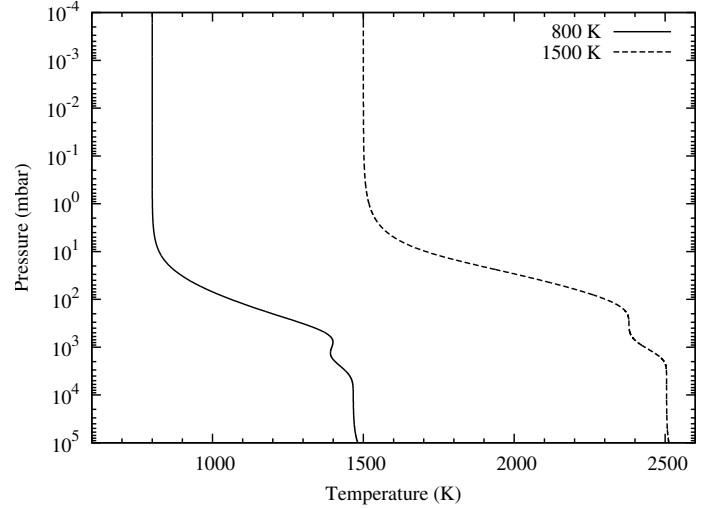


Fig. 8. Thermal profiles used in our thermo-photochemical model to study the impact of CO₂ high-temperature absorption cross sections.

4.1.2. Thermal profiles

We modelled two warm Neptunes with physical characteristics (mass and radius) similar to those of GJ 436b (Southworth 2010) and with equilibrium temperatures of 1091 K and 2043 K, which lead to temperatures of 800 K and 1500 K, respectively, in the upper part of the atmosphere above 10 mbars (Fig. 8). To construct the thermal profiles, we used the analytical model of Parmentier et al. (2015), with opacities from Valencia et al. (2013) and other opacities representing stellar light absorption and non-grey thermal effects adjusted to reproduce numerical models similar to those of Fortney et al. (2005). We did not include TiO and VO in the calculation of the radiative transfer. We note that at equilibrium temperatures less than ~ 1800 – 1900 K, the low gaseous abundance of TiO and VO, due to their cold trap in the deep atmospheric layers, has no effect on the thermal structure (Fortney et al. 2008; Parmentier et al. 2016). The chemical composition was assumed to be solar, which is not consistent with the atmospheric metallicity ($100 \times$ solar) we used in our model. However, as the purpose of this application is not to reproduce a real planet and its observations, but simply to see the effect of the different absorption cross sections of CO₂, we did not try to calculate more realistic thermal profiles. Furthermore, a thermal profile consistent with a high metallicity would have a higher temperature in the deep atmosphere, but the temperature in the upper atmosphere (for $P < 1$ mbar) would remain the same (Lewis et al. 2010; Agúndez et al. 2014).

4.1.3. Stellar irradiation

We chose a star emitting a high flux in the range (130–230 nm): HD 128167 (stellar type F2V). The stellar spectrum was constructed with observational data of HD 128167 for $\lambda \in (115$ – 900 nm) (Segura et al. 2003). For $\lambda \in (1$ – 114 nm) we used the solar spectrum (Thuillier et al. 2004) that we scaled to the radius and temperature of HD 128167 (i.e. $R_{\star} = 1.434 R_{\odot}$ and $T_{\star} = 6723$ K) in order to have a luminosity consistent with the physical parameters of the star. To obtain a stellar irradiation consistent with the equilibrium temperatures 1091 K and 2043 K, we set the semi-major axis to 0.126 AU and 0.036 AU, respectively. In Venot et al. (2013), we used three different stars (F, G, and M) and observed more variations of chemical abundances with the F star than with the two other

stars. Thus, here we limit our present study to this spectral type only.

4.1.4. Eddy diffusion coefficient

For the vertical mixing, we considered a constant eddy coefficient $K_{zz} = 10^8 \text{ cm}^2 \text{ s}^{-1}$. This value is often used in 1D photochemical models and corresponds to an average value deduced from 3D Global Circulation Models (GCMs) when the vertical scale height is multiplied by the root mean square of the vertical velocity. To date, no consensus exists on the best method to express the vertical mixing in 1D models and [Parmentier et al. \(2013\)](#) showed that the eddy diffusion coefficient can vary by two orders of magnitude depending on the method chosen.

4.1.5. CO₂ absorption cross sections

We modelled the warm Neptunes described above using absorption cross sections of CO₂ presented in this paper. For the planet with a temperature of 800 K in the upper atmosphere, we used (a) the absorption cross section at ambient temperature: $\sigma_{\text{CO}_2}(\lambda, 300)$, (b) the absorption cross section at 800 K: $\sigma_{\text{CO}_2}(\lambda, 800)$, and (c) the continuum of absorption extrapolated with Eq. (3) at 800 K: $\sigma_{\text{cont}}(\lambda, 800)$. For the warmer planet, with a temperature of 1500 K at the top of the atmosphere, we used (a) $\sigma_{\text{CO}_2}(\lambda, 300)$ and (b) the continuum of absorption calculated with Eq. (3) at 1500 K: $\sigma_{\text{cont}}(\lambda, 1500)$. All the absorption cross sections have been binned to a resolution $\Delta\lambda = 1 \text{ nm}$ in order to optimise the computational time. Doing so, the fine structure of the absorption (visible in Fig. 1) is smoothed. Stellar absorption due to the other molecules was calculated using data at the highest temperature available in the literature, which is often between 300 and 400 K. The references concerning the absorption cross sections and the quantum yields of photodissociation can be found in [Venot et al. \(2012\)](#) and [Dobrijevic et al. \(2014\)](#). The use of these mid-temperature data is the main source of uncertainty in our atmospheric modelling. It should be kept in mind that the atmospheric compositions presented in Figs. 12 and 14 might be different in reality. Here, our main interest is to show the influence of the hot CO₂ absorption cross sections.

4.1.6. CO₂ photodissociation rates

Under stellar irradiation, CO₂ has two routes to photodissociate:



The favoured route depends on the energy of the photons, according to the quantum yields presented in Table 2 ([Huebner et al. 1992](#)). These data have been measured at room temperature, but in the absence of data at higher temperature, we assume the same values at 800 K and 1500 K.

The loss rate of CO₂, due to photolysis only, is given by

$$L_{\text{CO}_2}^{\text{phot}} = \sum_{k=1,2} -J_k(z, T)n_{\text{CO}_2}, \quad (12)$$

where n_{CO_2} is the density of CO₂ (cm^{-3}) and $J_k(z, T)$ are the photodissociation rates of CO₂ (s^{-1}). The photodissociation rate depends on the absorption cross section of CO₂, $\sigma_{\text{CO}_2}(\lambda, T)$ (cm^2); the actinic photon flux, $F(\lambda, z, T)$ ($\text{cm}^{-2} \text{ s}^{-1} \text{ nm}^{-1}$); and the quantum yield corresponding to the route k , $q_k(\lambda)$ through

Table 2. Quantum yields for the photodissociations of carbon dioxide.

Quantum yield	Values [wavelength range]
$q_1(\lambda)$	1 [167–227]; 0 elsewhere
$q_2(\lambda)$	variable [50–107]; 1 [108–166]; 0 elsewhere

the equation

$$J_k(z, T) = \int_{\lambda_1}^{\lambda_2} \sigma_{\text{CO}_2}(\lambda, T) F(\lambda, z, T) q_k(\lambda) d\lambda, \quad (13)$$

where $[\lambda_1; \lambda_2]$ is the spectral range on which CO₂ absorbs the UV flux.

CO₂ interacting chemically with other species in the atmosphere, the global variation of CO₂ abundance over time is determined by the continuity equation

$$\frac{\partial n_i}{\partial t} = P_i - L_i - \text{div}(\Phi_i \mathbf{e}_z), \quad (14)$$

where P_i is the total production rate for a species i ($\text{cm}^{-3} \text{ s}^{-1}$), L_i its total loss rate ($\text{cm}^{-3} \text{ s}^{-1}$), and Φ_i its vertical flux ($\text{cm}^{-2} \text{ s}^{-1}$), which follows the diffusion equation.

This continuity equation governs the evolution of abundances of every molecules present in the atmosphere. Thus, all species are linked through a complex non-linear system of differential equations.

4.1.7. Synthetic transmission spectra

For the different atmospheric compositions determined with the 1D kinetic model, we computed synthetic infrared transmission spectra in the wavelength range 0.4–25 μm using the code Tau-REx ([Waldmann et al. 2015b,a](#)) in forward mode, which allows variable pressure-dependent temperature profiles. A discussion on the effect of isothermal vs. non-isothermal profiles can be found in [Rocchetto et al. \(2016\)](#). The infrared absorption cross sections of the absorbing species were computed using the linelists from ExoMol ([Tennyson & Yurchenko 2012](#)), HITRAN ([Rothman et al. 2009, 2013](#)), and HITEMP ([Rothman et al. 2010](#)). The absorbing species considered are C₂H₂, CO₂, HCN, NH₃, CH₄, CO, and H₂O. We considered collision-induced absorption of H₂-H₂ and H₂-He ([Rothman et al. 2009, 2013](#)) and assumed that the atmosphere is cloud-free. The spectrum shown was binned to a spectral resolution $R = \lambda/\Delta\lambda$, constant in wavelength, of 300.

4.2. Results

4.2.1. Photodissociation rates

We represented in Fig. 9 the total loss rate of CO₂ as well as the loss rates due to the photodissociations J_1 and J_2 for our different atmospheric models. Changing the absorption cross section of CO₂ modifies the total loss rate of CO₂, and the loss rates due to the photodissociations J_1 and J_2 . When using $\sigma_{\text{CO}_2}(\lambda, 800)$ instead of $\sigma_{\text{CO}_2}(\lambda, 300)$ the loss rate of J_2 grows by a factor of ~ 2.5 at 2×10^{-3} mbar. However, the major change is observed for J_1 , which has a loss rate multiplied by ~ 1200 at 0.1 mbar, when using the warm absorption cross section. Figure 10 shows that with $\sigma_{\text{CO}_2}(\lambda, 800)$, the stellar irradiation (for $\lambda < 230 \text{ nm}$) penetrates less deeply in the atmosphere because CO₂ absorbs more

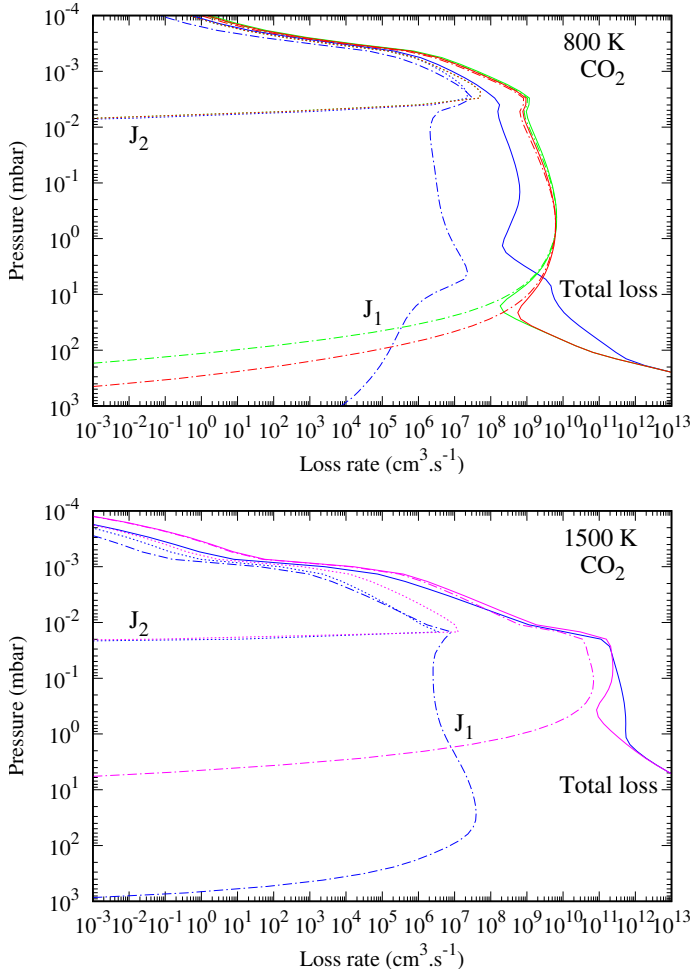


Fig. 9. For CO₂, total loss rates (full line) and loss rates due to photolysis J₁ (dot-dashed line) and J₂ (dotted line) in the two atmospheric models: 800 K (top) and 1500 K (bottom). Colours correspond to the different absorption cross section used: $\sigma_{\text{CO}_2}(\lambda, 300)$ (blue), $\sigma_{\text{CO}_2}(\lambda, 800)$ (red), $\sigma_{\text{cont}}(\lambda, 800)$ (green), and $\sigma_{\text{cont}}(\lambda, 1500)$ (pink).

incoming flux with the warm absorption cross section than with the 300 K one. Thus, the loss rate of J₁ decreases for pressures higher than 20 mbar and is finally less important than in the model with $\sigma_{\text{CO}_2}(\lambda, 300)$ for $P > 100$ mbar. However, at such pressures, the total loss rate of CO₂ is no longer due to the photodissociations. It is at low pressures that the contribution of the photodissociations is important for the total loss rate. In the model using $\sigma_{\text{CO}_2}(\lambda, 800)$, the loss due to J₁ represents more than 90% of the total loss of CO₂ (for $P < 20$ mbar), whereas this photodissociation has only a minor contribution to the total loss rate of CO₂ (0.5%) when using $\sigma_{\text{CO}_2}(\lambda, 300)$. The total loss rate of CO₂ increases when $\sigma_{\text{CO}_2}(\lambda, 800)$ is used in the model. For instance, at 0.5 mbar, it has been multiplied by ~ 18 .

Comparison between the results obtained with the experimental data and our parameterisation is satisfying. One can see that the differences in the loss rates are quite small between the models using $\sigma_{\text{CO}_2}(\lambda, 800)$ and $\sigma_{\text{cont}}(\lambda, 800)$. For the loss rate of J₂, the deviation is 3% at 2×10^{-3} mbar. For J₁ the deviation is 3% at 1 mbar, but increases as long as the pressure increases. It reaches $\sim 70\%$ at 10 mbar and 100% at 100 mbar. As the photodissociation J₁ is a major actor in the destruction of CO₂, the total loss rate is thus also different. The maximum difference is 74% at 16 mbar. For higher pressures, the contribution of the photodissociations to the total loss of CO₂ is negligible,

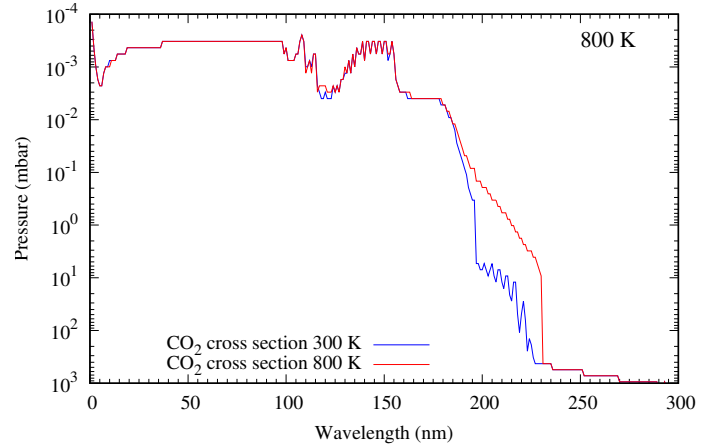


Fig. 10. Penetration of the stellar flux in the atmosphere labelled “800 K” when using $\sigma_{\text{CO}_2}(\lambda, 300)$ (blue) and $\sigma_{\text{CO}_2}(\lambda, 800)$ (red). It represents the level where the optical depth $\tau = 1$ in function of wavelength.

and the total loss rate is the same whether we use $\sigma_{\text{CO}_2}(\lambda, 800)$ or $\sigma_{\text{cont}}(\lambda, 800)$.

Unlike the previous case around 800 K, when we compared the models using $\sigma_{\text{CO}_2}(\lambda, 1500)$ and $\sigma_{\text{CO}_2}(\lambda, 300)$, we found that the total loss rate of CO₂ undergoes only slight modifications. The total loss rate of CO₂ is even lower by a factor 6 at 0.37 mbar because of the loss rates of other chemical reactions, whose contributions to the total loss rate are not shown. Qualitatively, we observe the same behaviour as for the atmosphere at 800 K. In the upper atmosphere, the loss rates of J₂ and J₁ increase when the warmer absorption cross section is used. We found that the loss rate of J₁ begins to decrease for lower pressures in the model using $\sigma_{\text{CO}_2}(\lambda, 1500)$ rather than $\sigma_{\text{CO}_2}(\lambda, 300)$. Quantitatively, however, there is an important difference with the model at 800 K. At 800 K the photodissociation J₁ is responsible (more than 90%) for the destruction of CO₂ in the upper atmosphere; instead, at 1500 K the contribution of the photodissociation is less important. At 0.1 mbar, $\sim 32\%$ of the loss rate of CO₂ is due to the photodissociation J₁. Thus, even if this contribution is much more important than when using $\sigma_{\text{CO}_2}(\lambda, 300)$ (where it represents only $7 \times 10^{-4}\%$), we do not expect the increase in the loss rate of J₁ to be sufficient to significantly impact the abundance of CO₂ in this very hot atmosphere.

We see that using the warm absorption cross sections of CO₂ increases the role of photolysis in the destruction of CO₂, which in some cases can even become the dominant process in the high atmosphere. Consequently, the actinic flux is impacted (see Fig. 10), which in turn modifies the photodissociation rates of other absorbing molecules such as NH₃ and CH₄ (through Eq. (13), applied to other species). To illustrate this phenomenon of shielding, we present in Fig. 11 the total loss rate of ammonia and the loss rate due to its single photodissociation route, $\text{NH}_3 + h\nu \rightarrow \text{NH}_2 + \text{H}$ (J₃). Although the absorption cross section of ammonia has not been modified between the different models, but only that of CO₂, the loss rates of NH₃ are impacted. With the hot absorption cross sections ($\sigma_{\text{CO}_2}(\lambda, 800)$, $\sigma_{\text{cont}}(\lambda, 800)$ and $\sigma_{\text{CO}_2}(\lambda, 1500)$), photodissociation of NH₃ occurs less than with $\sigma_{\text{CO}_2}(\lambda, 300)$. For the atmosphere at 800 K, the maximum of J₃ loss rates is shifted from 7 mbar to ~ 1.5 mbar, and from 50 mbar to 0.4 mbar for the atmosphere at 1500 K. Consequently, we expect that many molecules in addition to CO₂ will have their abundances modified. This phenomenon of shielding is further increased by the fact that

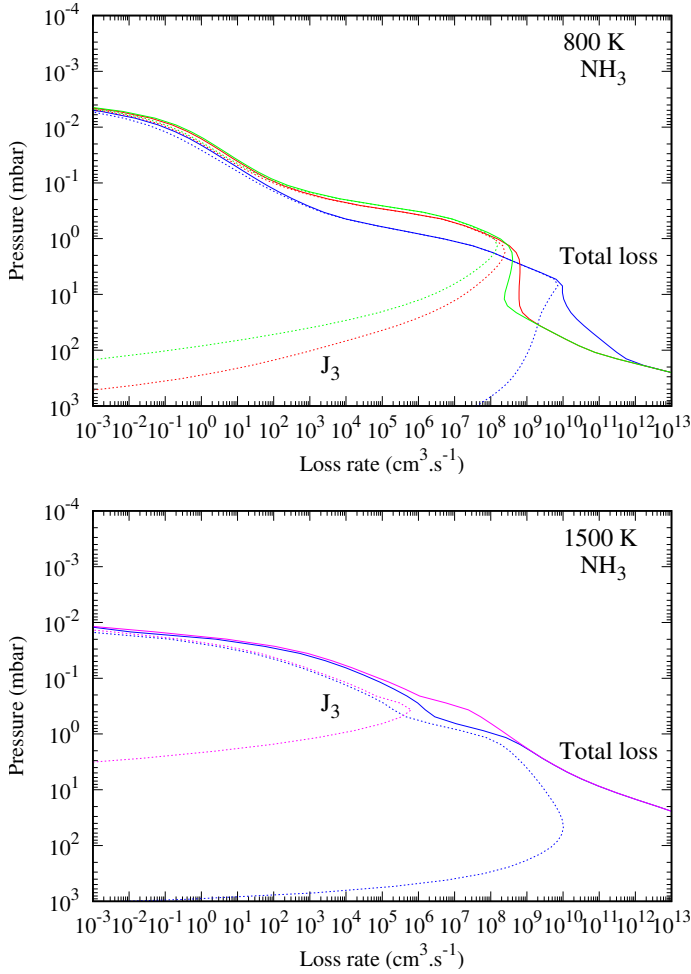


Fig. 11. For NH_3 , total loss rates (full line) and loss rates due to photolysis J_3 (dotted line) in the two atmospheric models: 800 K (top) and 1500 K (bottom). Colours correspond to the different absorption cross section used: $\sigma_{\text{CO}_2}(\lambda, 300)$ (blue), $\sigma_{\text{CO}_2}(\lambda, 800)$ (red), $\sigma_{\text{cont}}(\lambda, 800)$ (green), and $\sigma_{\text{cont}}(\lambda, 1500)$ (pink).

the abundances of species are determined by a system of coupled differential equations. Thereby, each variation of abundance of one single species affects the species with which it reacts chemically.

4.2.2. Chemical composition

For the 800 K atmosphere, we represented in Fig. 12 the vertical mixing ratios of CO_2 and H_2O (as these species contribute the most to the transmission spectra, see Sect. 4.2.3), as well as the mixing ratios of the nine molecules that are the most affected by the change of $\sigma_{\text{CO}_2}(\lambda, T)$, amongst species with a mixing ratio higher than 10^{-10} . These results confirm what was expected looking at the loss rates: changing the absorption cross section of CO_2 affects the abundance of numerous species, not only CO_2 . The modification of the absorption cross section of CO_2 has an impact on the atmosphere down to pressure levels of 0.6 bar. Qualitatively, with $\sigma_{\text{CO}_2}(800, T)$ the vertical profiles are shifted to lower pressures. For a given pressure level, it results in lower abundances than with $\sigma_{\text{CO}_2}(300, T)$ for CO_2 , H , and OH , and higher abundances for CH_4 , NH_3 , and HCN . The other species (CH_3 , NO , NH_2 , and N_2O) having tortuous vertical profiles, the direction of the change (i.e. increase or decrease) in the abundances depends on the pressure level. For NH_3 , there is

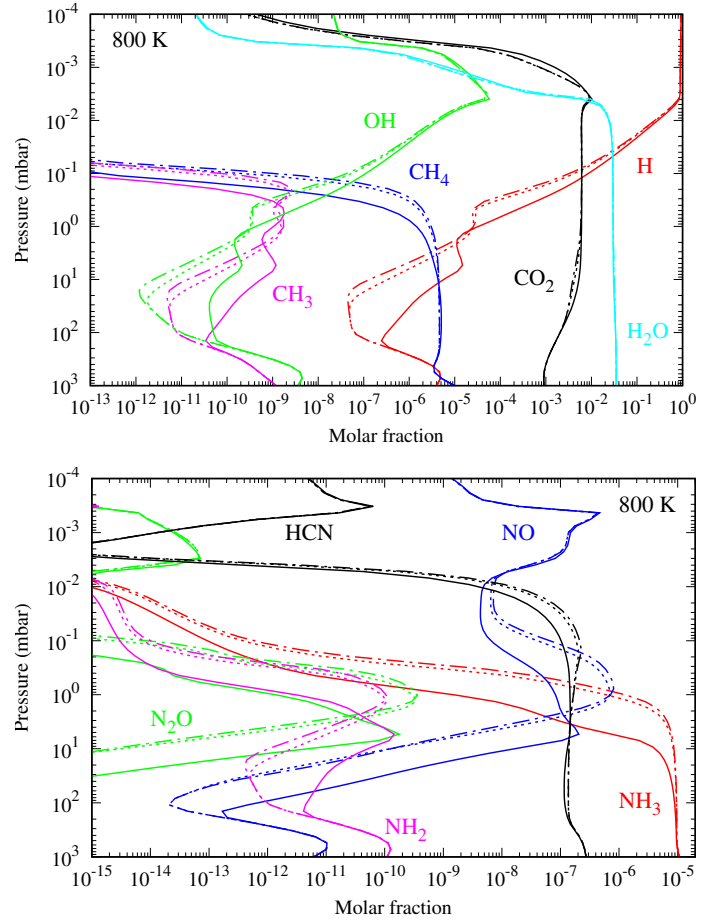


Fig. 12. Vertical mixing ratios of CO_2 and ten selected molecules computed with the photochemical model using $\sigma_{\text{CO}_2}(\lambda, 300)$ (full line), $\sigma_{\text{CO}_2}(\lambda, 800)$ (dotted line), and $\sigma_{\text{cont}}(\lambda, 800)$ (dot-dashed line) for the thermal profile labelled “800 K”.

a correspondence between the loss rate (Fig. 11) and the vertical profiles (Fig. 12). As has been said in Sect. 4.2.1, the maximum of J_3 loss rate varied from 7 mbar, with $\sigma_{\text{CO}_2}(300, T)$, to ~ 1.5 mbar, with $\sigma_{\text{CO}_2}(800, T)$. These pressures correspond to the respective levels where the removal of ammonia by photolysis is no longer dominant (if we go from low to high pressures) and NH_3 reaches an abundance of $\sim 3 \times 10^{-6}$, close to its value at deeper levels.

To quantify the change in composition induced by the warm CO_2 absorption cross section, we represented in Fig. 13 the relative deviation of abundances (i.e. $(y_i^{800} - y_i^{300})/y_i^{300} \times 100$, with y_i^T the molar fraction of the species i in the model using $\sigma_{\text{CO}_2}(\lambda, T)$) of the compounds shown in Fig. 12 regarding the pressure level. The compounds CH_4 and CH_3 show a large relative deviation of abundances at 0.1 mbar: $2.1 \times 10^5\%$ and $1 \times 10^5\%$, respectively. The abundance of NH_3 , N_2O , and NH_2 are also strongly modified with relative deviation of $1.9 \times 10^5\%$, $1.6 \times 10^5\%$, and $3 \times 10^4\%$, respectively, around 0.5 mbar. These values are ~ 150 – $300 \times$ higher than the maximum relative deviation of CO_2 at 3.2×10^{-4} mbar (i.e. -66%). Water is less affected with a maximum relative deviation of -46% at 4×10^{-3} mbar.

For the atmosphere at 800 K, we studied the deviation of the atmospheric composition induced by the use of the analytical formula (Eq. (3)) applied with $T = 800$ K, $\sigma_{\text{cont}}(\lambda, 800)$, instead of the experimental data $\sigma_{\text{CO}_2}(\lambda, 800)$. The atmospheric composition found with $\sigma_{\text{cont}}(\lambda, 800)$ is shown in Fig. 12. Deviations

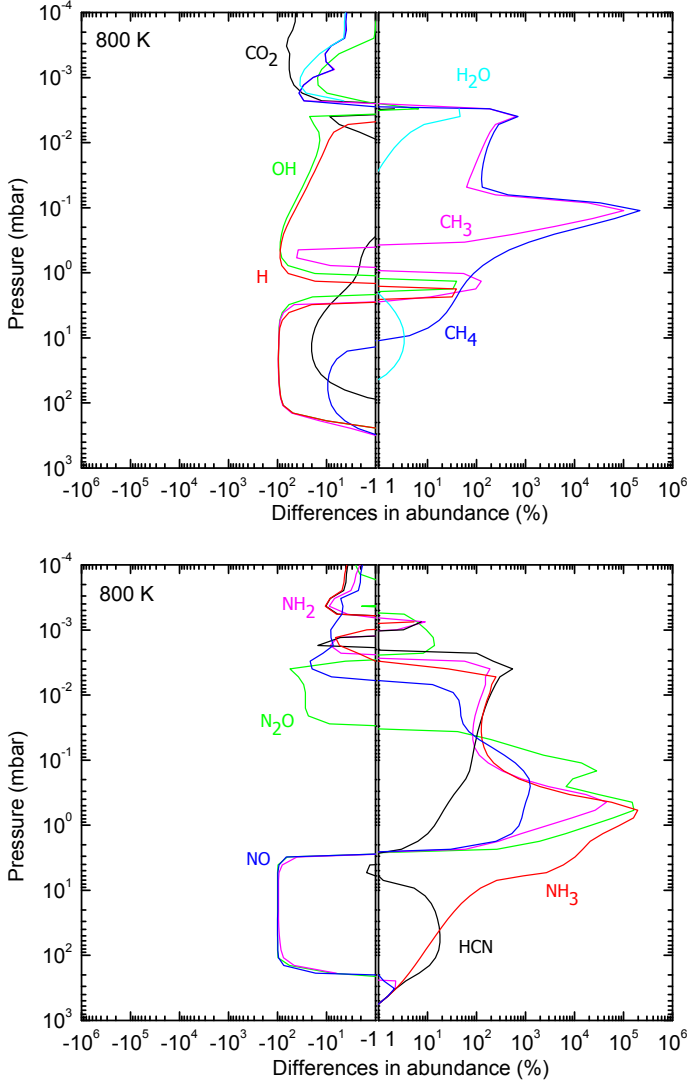


Fig. 13. Differences in abundances (%) between the results obtained using $\sigma_{\text{CO}_2}(\lambda, 800)$ and $\sigma_{\text{CO}_2}(\lambda, 300)$ for the thermal profile labelled “800 K”.

with the results obtained with $\sigma_{\text{CO}_2}(\lambda, 800)$ are negligible. We calculated the relative deviation of abundances (i.e. $(y_i^{800,\text{cont}} - y_i^{800})/y_i^{800} \times 100$) and found a maximum for CH₄ (500% at 0.08 mbar). However, in the case studied here, y_{CH_4} is less than 10^{-11} at this pressure level. Thus, this deviation will have no impact on the observable corresponding to this composition, the planetary synthetic spectrum (cf. Sect. 4.2.3).

For the atmosphere at 1500 K, the use of $\sigma_{\text{cont}}(\lambda, 1500)$ instead of $\sigma_{\text{CO}_2}(\lambda, 300)$ modifies to a smaller extent the chemical composition (Fig. 14). The vertical abundance profile of CO₂ is barely modified. Between 0.02 and 2 mbar, H and OH have lower abundances with the hot absorption cross section. As for the 800 K atmosphere, CH₄, NH₃, and HCN are destroyed less deep by photolysis than with $\sigma_{\text{CO}_2}(\lambda, 300)$. Compared to the 800 K atmosphere, the abundance of NO is much less modified by the change of CO₂ absorption cross section. The relative deviation of abundances (i.e. $(y_i^{1500,\text{cont}} - y_i^{300})/y_i^{300} \times 100$) are represented in Fig. 15. Amongst the species with mixing ratios $>10^{-10}$, NH₃ and HCN are the ones that experience the largest variations. The relative deviation of their abundance is $10^4\%$ at 0.37 mbar. For

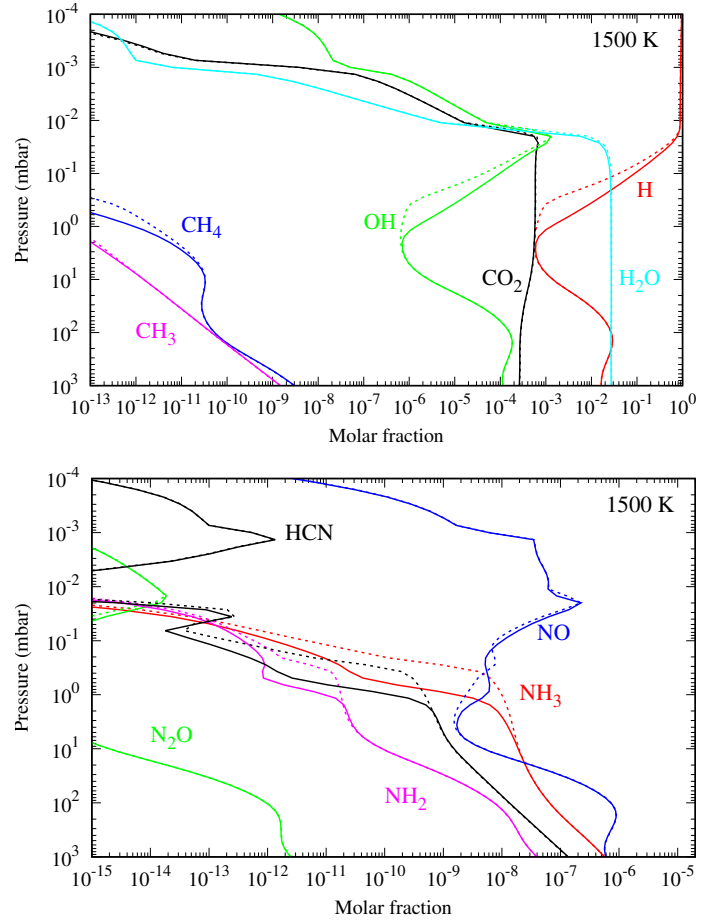


Fig. 14. Vertical mixing ratios of CO₂ and ten selected molecules computed with the photochemical model using $\sigma_{\text{CO}_2}(\lambda, 300)$ (full line) and $\sigma_{\text{cont}}(\lambda, 1500)$ (dotted line) for the thermal profile labelled “1500 K”.

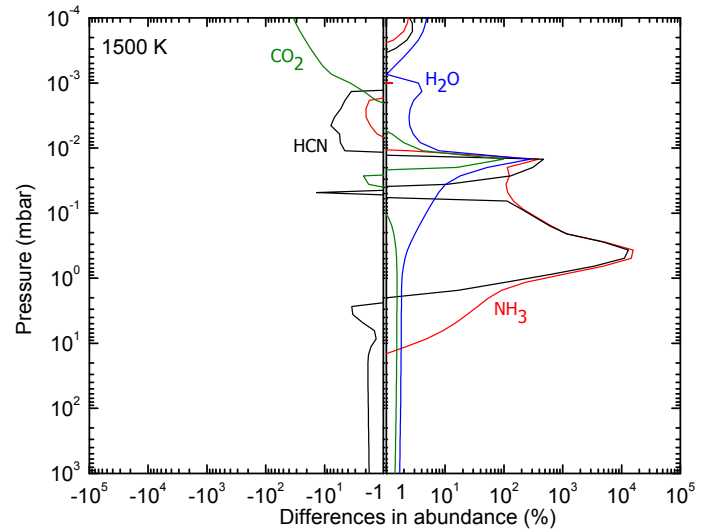


Fig. 15. Differences in abundances (%) between the results obtained using $\sigma_{\text{cont}}(\lambda, 1500)$ and $\sigma_{\text{CO}_2}(\lambda, 300)$, for the thermal profile labelled “1500 K”.

H₂O the relative deviation is 281% at 1.4×10^{-2} mbar. The other species present variations of less than 100%.

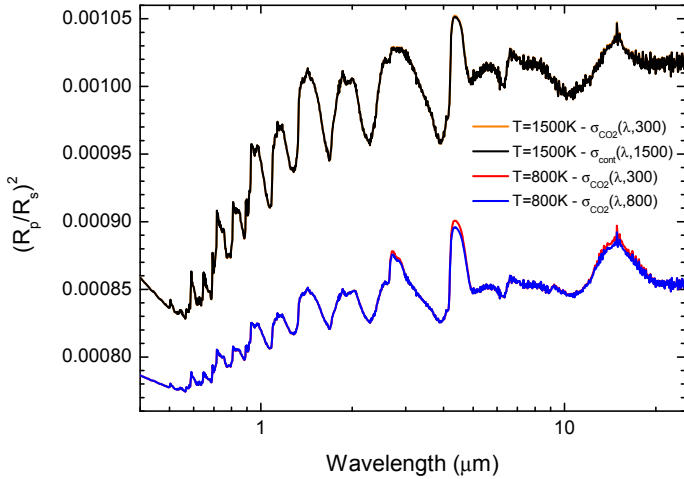


Fig. 16. Synthetic transmission spectra of the two warm Neptunes, corresponding to the chemical compositions calculated with $\sigma_{\text{CO}_2}(\lambda, 300)$ (red) and $\sigma_{\text{CO}_2}(\lambda, 800)$ (blue) for the 800 K atmosphere and with $\sigma_{\text{CO}_2}(\lambda, 300)$ (orange) and $\sigma_{\text{cont}}(\lambda, 1500)$ (black) for the 1500 K atmosphere. R_p and R_s are the planet and star radius, respectively. The spectrum shown was binned to a resolution (constant in λ) of $R = 300$.

4.2.3. Effect on observable

Infrared transmission spectra of the two warm Neptunes are presented in Fig. 16. For all of them, the absorption is dominated by H_2O except around 2.7, 4.3, and 14.9 μm , where CO_2 is the dominant absorbing species. We observed that the spectra of the 1500 K atmosphere present larger features and are shifted to larger planetary radii than the spectra of the colder atmosphere. This is due to the fact that the atmospheric scale height ($H = k_B T / \mu g$, where μ is the mean molecular weight) increases when the temperature increases, leading to a more extended atmosphere.

The differences between the spectra corresponding to the models using $\sigma_{\text{CO}_2}(\lambda, 300)$ and $\sigma_{\text{CO}_2}(\lambda, 800)$ are quite small. Variations are visible in the three CO_2 absorption bands. At 4.3 μm , the atmospheric absorption decreases by 5 ppm when using the warmer absorption cross section, which represents a decrease of 0.55%. At 14.9 μm , a decrease of 4.8 ppm (0.55%) is observed. Finally, a lower variation of 2.5 ppm (0.3%) is visible at 2.7 μm . These changes are below the level of uncertainty reached by recent observations of small planets in the size range of warm Neptunes/super-Earths (i.e. 60 ppm for Kreidberg et al. 2014; and 22 ppm for Tsiaras et al. 2016). Reaching such a high level of sensitivity seems to be a real challenge even for the future powerful JWST. Indeed, such a low S/N will be accessible, but observations in this wavelength range will in fact be limited by the systematics of the JWST, which are difficult to assess. They will probably be lower than the *Hubble* Space Telescope, i.e. about 20 ppm for the instruments Near Infrared Imager and Slitless Spectrograph (NIRISS) and Near Infrared Camera (NIRCAM; Rocchetto et al. 2016) and about 30 ppm for Mid-Infrared Instrument (MIRI; Beichman et al. 2014).

However, it should be kept in mind that these deviations are only due to the change in the VUV absorption cross section of one single species. Using hot VUV absorption cross sections for all the species present in the atmosphere will probably have more consequences on the atmospheric composition and thus could produce a larger effect on the transmission spectra. We also compared the spectra corresponding to the atmospheric compositions determined using $\sigma_{\text{CO}_2}(\lambda, 800)$ and $\sigma_{\text{cont}}(\lambda, 800)$. The variations are tiny. The maximum deviation occurs at 4.7 μm and

is 0.15 ppm (0.017%). This level of variation confirms that using the analytical formula of the continuum of absorption instead of the real absorption cross section is a good approximation.

For the warmer atmosphere, the change in atmospheric composition due to the different VUV absorption cross sections of CO_2 has almost no effect on the transmission spectrum. The most important deviation occurs at 4.7 μm and is 1 ppm, which represents a decrease of 0.1%. This variation is not detectable with current instruments, and it is highly probable that such a sensitivity will remain unreachable by future instruments during the next decades.

Figure 17 represents spectral transmittance as a function of pressure for the two atmospheres, when the warm CO_2 absorption cross sections have been used. It allows us to see which pressure regions (and therefore the temperatures in Fig. 8) are probed at different wavelengths for the two atmospheres. Generally, we notice that the same wavelength probes higher pressures in the 800 K atmosphere than in the 1500 K atmosphere. For the colder atmosphere, we see that the wavelengths for which we observe deviations between the spectra using $\sigma_{\text{CO}_2}(\lambda, 300)$ and $\sigma_{\text{CO}_2}(\lambda, 800)$, i.e. 2.5, 4.3, and 14.9 μm , correspond to the atmospheric layers between 10^{-3} and 4×10^{-3} mbar, which corresponds to the pressure levels where CO_2 exhibits a variation of $\sim 50\%$ and is more abundant than H_2O by more than one order of magnitude (Figs. 12 and 13). For the warmer atmosphere, the maximum variation between the spectra using different absorption cross sections is found at 4.7 μm . This wavelength probes the atmosphere around 10^{-2} mbar, which corresponds to a level where the abundance of CO_2 varies by $\sim 100\%$. Despite the larger magnitude of abundance deviation with respect to the 800 K atmosphere, the effect on the synthetic spectra is smaller because CO_2 is less abundant (by a factor 10) in the warmer atmosphere and has about the same abundance as H_2O , around 10^{-2} mbar. Therefore, the relative contribution of CO_2 to the planetary spectrum is lower than for the 800 K atmosphere.

5. Conclusion

We present ten experimental measurements of the VUV absorption cross section of CO_2 from 150 K to 800 K in the wavelength range 115–230 nm, which allow us to quantify the temperature dependency of this data. We study more specifically the evolution of the continuum of absorption and determine a parameterisation that depends only on the temperature and the wavelength. At temperatures higher than 500 K, using this parameterisation is a good approximation for the absorption of CO_2 because the contribution of the fine structure on the absorption is less than 20%.

We study the implication of these new data for exoplanet studies using our thermo-photochemical model. In atmospheres around 800 K, using the appropriate absorption cross sections of CO_2 modifies the abundances of many species by several orders of magnitude. In our model, molecules that undergo the greatest change are CH_4 , NH_3 , N_2O , and CH_3 . These changes lead to moderate deviations in transmission spectra (5 ppm) that would be hard to observe even with future instruments such as the JWST. In warmer atmospheres (~ 1500 K), using the appropriate CO_2 absorption cross sections has a lower impact on the atmospheric composition because the fast thermal kinetics dominates over the photodissociation processes in the area probed by observations. Thus, synthetic spectra are not impacted. We can therefore conclude that measurements at higher temperatures, higher than 1000 K, are not necessary in the context of warm exoplanet studies.

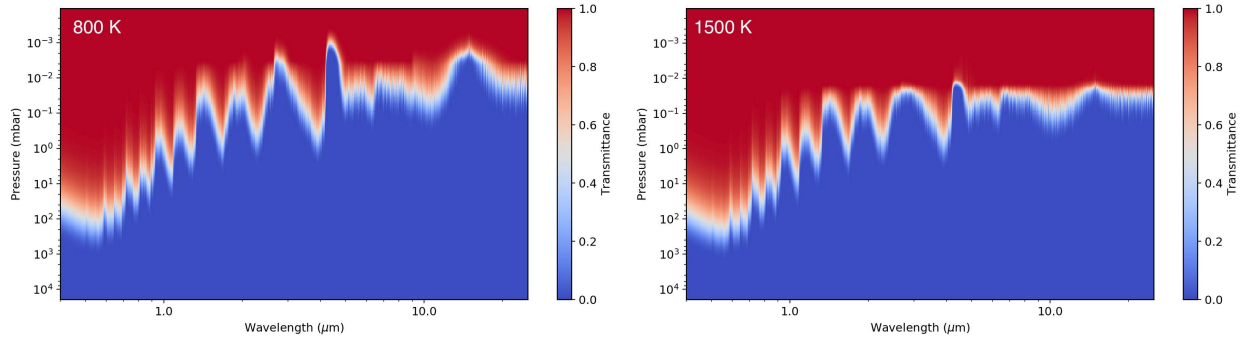


Fig. 17. Spectral transmittance as a function of pressure for the 800 K (left) and the 1500 K atmospheres (right). The plots correspond to the case where CO₂ absorption cross sections at respectively 800 K and 1500 K have been used.

We also compare the results obtained using the real absorption cross section and the continuum calculated using the parameterisation. Small differences are observed for the atmospheric composition, but they do not have visible implications for the synthetic spectra. This approximation can thus be used without any risk for atmospheres with temperatures higher than 500 K. For lower temperatures, the fine structure cannot be neglected, and a more detailed study of its variation with temperature will be the subject of a forthcoming paper.

It is worth noting that the changes observed in the atmospheric composition and the synthetic spectra are due to the change of only one parameter: the absorption cross section of CO₂. Given the high coupling that exists between all the molecules through chemical kinetics and the phenomenon of shielding, it remains necessary to determine high-temperature data for all absorbing species. Indeed, with the near launch of the JWST (Spring 2019), reducing the uncertainty on the results of atmospheric models is paramount to be able to interpret its future observations correctly.

Acknowledgements. The authors wish to thank the anonymous referee for the very interesting comments. They also thank Gerd Reichard and Peter Baumgärtel for their excellent assistance during the synchrotron radiation beam time periods. The authors also acknowledge the financial supports of the European Commission Programme “Access to Research Infrastructures” for providing access to the synchrotron facility BESSY in Berlin, of the programme PIR EPOV, and that of the CNRS/INSU Programme National de Planétologie (PNP). O.V. acknowledges support from the KU Leuven IDO project IDO/10/2013, from the FWO Postdoctoral Fellowship programme, and from the Postdoctoral Fellowship programme of the Centre National d’Études Spatial (CNES). I.P.W. acknowledges support by the ERC project ExoLights (617119).

References

- Agúndez, M., Venot, O., Selsis, F., & Iro, N. 2014, *ApJ*, **781**, 68
 Asplund, M., Grevesse, N., Sauval, A. J., & Scott, P. 2009, *ARA&A*, **47**, 481
 Beichman, C., Benneke, B., Knutson, H., et al. 2014, *PASP*, **126**, 1134
 Cossart-Magos, C., Jungen, M., & Launay, F. 1987, *Mol. Phys.*, **61**, 1077
 Dobrijevic, M., Hébrard, E., Loison, J. C., & Hickson, K. M. 2014, *Icarus*, **228**, 324
 Ferradaz, T., Bénilan, Y., Fray, N., et al. 2009, *Planet. Space Sci.*, **57**, 10
 Fortney, J. J., Marley, M. S., Lodders, K., Saumon, D., & Freedman, R. 2005, *ApJ*, **627**, L69
 Fortney, J. J., Lodders, K., Marley, M. S., & Freedman, R. S. 2008, *ApJ*, **678**, 1419
 Fortney, J. J., Mordasini, C., Nettelmann, N., et al. 2013, *ApJ*, **775**, 80
 Fortney, J. J., Robinson, T. D., Domagal-Goldman, S., et al. 2016, ArXiv e-prints [arXiv:1602.06305]
 Grebenshchikov, S. Y. 2013, *J. Chem. Phys.*, **138**, 224107
 Grebenshchikov, S. Y. 2016, *Journal of CO₂ Utilization*, **15**, 32
 Herzberg, G. 1989, *Molecular Spectra and Molecular Structure: I. Spectra of diatomic molecules, Molecular Spectra and Molecular Structure* (R.E. Krieger Publishing Company)
- Huebner, W., Keady, J., & Lyon, S. 1992, *Solar photo rates for planetary atmospheres and atmospheric pollutants* (Kluwer Academic Pub.)
 Jensen, R., Guettler, R., & Lyman, J. 1997, *Chem. Phys. Lett.*, **277**, 356
 Kreidberg, L., Bean, J. L., Desert, J.-M., et al. 2014, *Nature*, **505**, 69
 Lefèvre, F., Lebonnois, S., Montmessin, F., & Forget, F. 2004, *J. Geophys. Res. Planets*, **109**, E07004
 Lewis, B., & Carver, J. 1983, *J. Quant. Spectr. Rad. Transf.*, **30**, 297
 Lewis, N. K., Showman, A. P., Fortney, J. J., et al. 2010, *ApJ*, **720**, 344
 Liang, M., Parkinson, C., Lee, A., Yung, Y., & Seager, S. 2003, *ApJ*, **596**, L247
 Liang, M., Seager, S., Parkinson, C., Lee, A., & Yung, Y. 2004, *ApJ*, **605**, L61
 Madhusudhan, N., & Seager, S. 2009, *ApJ*, **707**, 24
 Madhusudhan, N., Harrington, J., Stevenson, K. B., et al. 2011, *Nature*, **469**, 64
 Montmessin, F., Bertaux, J.-L., Lefèvre, F., et al. 2011, *Icarus*, **216**, 82
 Moses, J. I., Line, M. R., Visscher, C., et al. 2013, *ApJ*, **777**, 34
 Oehlschlaeger, M., Davidson, D., Jeffries, J., & Hanson, R. 2004, *Chem. Phys. Lett.*, **399**, 490
 Parkinson, W. H., Rufus, J., & Yoshino, K. 2003, *Chem. Phys.*, **290**, 251
 Parmentier, V., Showman, A. P., & Lian, Y. 2013, *A&A*, **558**, A91
 Parmentier, V., Guillot, T., Fortney, J. J., & Marley, M. S. 2015, *A&A*, **574**, A35
 Parmentier, V., Fortney, J. J., Showman, A. P., Morley, C., & Marley, M. S. 2016, *ApJ*, **828**, 22
 Rocchetto, M., Waldmann, I. P., Venot, O., Lagage, P.-O., & Tinetti, G. 2016, *ApJ*, **833**, 120
 Rothman, L. S., Gordon, I. E., Barbe, A., et al. 2009, *J. Quant. Spectr. Rad. Transf.*, **110**, 533
 Rothman, L. S., Gordon, I. E., Barber, R. J., et al. 2010, *J. Quant. Spectr. Rad. Transf.*, **111**, 2139
 Rothman, L. S., Gordon, I. E., Babikov, Y., et al. 2013, *J. Quant. Spectr. Rad. Transf.*, **130**, 4
 Schinke, R. 1995, *Photodissociation dynamics: spectroscopy and fragmentation of small polyatomic molecules No. 1* (Cambridge University Press)
 Schulz, C., Koch, J., Davidson, D., Jeffries, J., & Hanson, R. 2002, *Chem. Phys. Lett.*, **355**, 82
 Segura, A., Krellove, K., Kasting, J., et al. 2003, *Astrobiol.*, **3**, 689
 Smith, M. D. 2004, *Icarus*, **167**, 148
 Southworth, J. 2010, *MNRAS*, **408**, 1689
 Stark, G., Yoshino, K., Smith, P. L., & Ito, K. 2007, *J. Quant. Spectr. Rad. Transf.*, **103**, 67
 Swain, M. R., Tinetti, G., Vasisht, G., et al. 2009a, *ApJ*, **704**, 1616
 Swain, M. R., Vasisht, G., Tinetti, G., et al. 2009b, *ApJ*, **690**, L114
 Tennyson, J., & Yurchenko, S. N. 2012, *MNRAS*, **425**, 21
 Thuillier, G., Floyd, L., Woods, T., et al. 2004, *Adv. Space Res.*, **34**, 256
 Tsiaras, A., Rocchetto, M., Waldmann, I. P., et al. 2016, *ApJ*, **820**, 99
 Valencia, D., Guillot, T., Parmentier, V., & Freedman, R. S. 2013, *ApJ*, **775**, 10
 Venot, O., Hébrard, E., Agúndez, M., et al. 2012, *A&A*, **546**, A43
 Venot, O., Fray, N., Bénilan, Y., et al. 2013, *A&A*, **551**, A131
 Waldmann, I. P., Rocchetto, M., Tinetti, G., et al. 2015a, *ApJ*, **813**, 13
 Waldmann, I. P., Tinetti, G., Rocchetto, M., et al. 2015b, *ApJ*, **802**, 107
 Yoshino, K., Esmond, J. R., Sun, Y., et al. 1996, *J. Quant. Spectr. Rad. Transf.*, **55**, 53
 Zasova, L. V., Ignatiev, N., Khatuntsev, I., & Linkin, V. 2007, *Planet. Space Sci.*, **55**, 1712
 Zuev, A., & Starikovskii, A. Y. 1990, *J. Appl. Spectr.*, **52**, 304